Article

Synthesis and Evaluation of [64Cu]Cu-NOTA-HFn for PET Imaging of Transferrin Receptor 1 Expression in Nasopharyngeal Carcinoma

Yanfang Shen, Renwei Zhou, Lei Bi, Guolong Huang, Min Yang, Zhijun Li, Jijin Yao, Jianzhong Xian, Yifan Qiu, Peizhen Ye, Yongshan Liu, Yuyi Hou, Hongjun Jin,* and Ying Wang*

Cite This: ACS Omega 2024, 9, 17423−17431

Read Online

ACCESS | Metrics & More | Article Recommendations | Supporting Information

ABSTRACT: As recurrent and metastatic nasopharyngeal carcinoma (NPC) is the most common cause of death among patients with NPC, there is an urgent clinical need for the development of precision diagnosis to guide personalized treatment. Recent emerging evidence substantiates the increased expression of transferrin receptor 1 (also known as cluster of differentiation 71, CD71) within tumor tissues and the inherent targeting capability of natural heavy-chain ferritin (HFn) toward CD71. This study aimed to synthesize and assess a radiotracer ([64Cu]Cu-NOTA-HFn) designed to target CD71 for positron emission tomography (PET) imaging in an NPC tumor-bearing mouse model. The entire radiolabeling process of [64Cu]Cu-NOTA-HFn was completed within 15 min with high yield (>98.5%) and high molar activity (72.96 ± 21.33 GBq/μmol). The in vitro solubility and stability experiments indicated that [64Cu]Cu-NOTA-HFn had a high water solubility ($\log P = -2.42 \pm 0.52$, $n = 6$) and good stability in phosphate-buffered saline (PBS) for up to 48 h. The cell saturation binding assay indicated that [64Cu]Cu-NOTA-HFn had a nanomolar affinity ($K_d = 10.9 \pm 6.1$ nM) for CD71-overexpressing C666-1 cells. To test the target engagement in vivo, prolonged-time PET imaging was performed at 1, 6, 12, 24, and 36 h postinjection (p.i.) of [64Cu]Cu-NOTA-HFn to C666-1 NPC tumor-bearing mice. The C666-1 tumors could be visualized by [64Cu]Cu-NOTA-HFn and blocked by nonradiolabeled HFn. PET imaging quantitative analysis demonstrated that the uptake of [64Cu]Cu-NOTA-HFn in C666-1 tumors peaked at 6 h p.i. and the best radioactive tumor-to-muscle ratio was 10.53 ± 3.11 ($n = 3$). Ex vivo biodistribution assay at 6 h p.i. showed that the tumor uptakes were 1.43 ± 0.23%ID/g in the nonblock group and 0.92 ± 0.2%ID/g in the block group ($n = 3$, $p < 0.05$). Immunohistochemistry and immunofluorescence staining confirmed positive expression of CD71 and the uptake of HFn in C666-1 tumor tissues. In conclusion, our experiments demonstrated that [64Cu]Cu-NOTA-HFn possesses a very high target engagement for CD71-positive NPC tumors and provided a fundamental basis for further clinical translation.
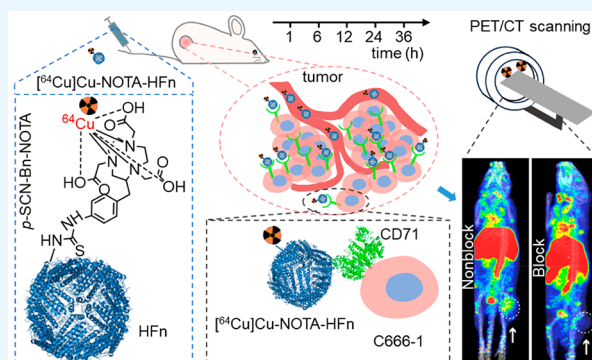
1. INTRODUCTION

Nasopharyngeal carcinoma (NPC) exhibits a higher prevalence in East Asia and Southeast Asia.[1] Histologically, it can be categorized into three main subtypes: keratinizing squamous cell carcinoma, nonkeratinizing squamous cell carcinoma, and basaloid squamous cell carcinoma, with the nonkeratinizing subtype further dividing into differentiated and undifferentiated forms.[2] In high-incidence regions, undifferentiated nonkeratinizing squamous cell carcinoma predominates, accounting for approximately 95% of cases and displaying a notably increased tendency for distant metastasis.[3] Undifferentiated NPC responds well to combined radiotherapy and chemotherapy, resulting in a notable 5-year local control rate of over 80%.[4] However, intratumoral heterogeneity, with variable molecular characteristics within the tumor, leads to different responses to these treatments.[5] This heterogeneity contributes to treatment resistance, recurrence, and metastasis in approximately 15−30% of patients. Among these patients,

the median survival time is only 11−28 months.[4] Consequently, there exists an urgent need to develop both specific diagnostic methods and effective therapeutic interventions for NPC.

The current standard diagnostic approach for NPC involves invasive nasopharyngoscopy to biopsy suspicious lesions, but this method is constrained to the nasopharynx and may result in potential false negatives.[6] Although conventional anatomical imaging methods like CT, MRI, and ultrasound are valuable for morphological assessment, they are unable to provide insights into the molecular characteristics within the tumor.[7]

Molecular imaging techniques offer the potential for early diagnosis and personalized treatment guidance by tracking tumor-related molecular events.[8] Among these methods, positron emission tomography (PET) is a well-established and promising approach. It uses radiolabeled ligands to target specific molecules with high sensitivity, enabling noninvasive visualization and quantitative analysis of these molecular markers.[9] Overexpressed receptors on tumor cell surfaces play a crucial role in early tumorigenesis, making them ideal targets for diagnosis and therapy.[10,11] Hence, the exploration of overexpressed cell membrane receptors in NPC and the use of radiolabeled ligands offer the potential to achieve early and precise diagnosis of NPC and facilitate personalized treatment.

Transferrin receptor 1 (also known as cluster of differentiation 71, CD71), is a type II transmembrane glycoprotein located on the cell membrane that mediates the cellular iron uptake.[12] CD71 is typically expressed at low levels in most normal cells but has been reported to be overexpressed in various malignant tumors[13] and plays an important role in tumor proliferation, migration, and invasion.[14,15] Furthermore, its association with clinical staging and prognosis has been confirmed in studies,[16−18] solidifying its status as a versatile tumor marker. We observed that CD71 was overexpressed in human NPC tissues, and its expression was higher in metastatic foci compared to the primary lesions in matched patients (unpublished study to date). It has also been reported in the literature that CD71 is highly expressed in NPC tissues.[19] CD71 has various binders available for use, such as CD71 antibodies,[20] transferrin (Tf),[21] and heavy-chain ferritin (H-ferritin, HFn).[22] Among these, HFn serves as a natural ligand with excellent biocompatibility and inherent targeting specificity for CD71, while its 24 subunits can self-assemble to enable controlled drug encapsulation and release.[23] Compared to other binders, HFn exhibits threshold-dependent internalization upon binding to CD71, enhancing its in vivo tumor selectivity and biosafety.[23,24] Furthermore, the binding sites of HFn to CD71 are distinct from those of Tf,[22] thus the use of HFn minimally interferes with the physiological process of cellular iron acquisition mediated by Tf binding to CD71. Therefore, HFn emerges as the optimal ligand for CD71. In this study, we intend to use radiolabeled HFn to validate the potential of HFn in monitoring the expression of CD71 and visualizing NPC lesions.

To achieve a favorable target-to-nontarget ratio, the selection of a radionuclide with a half-life similar to that of HFn is crucial. Previous research has indicated that HFn exhibits a blood clearance half-life of approximately 4 h,[25] while the β^+ emitter copper-64 is well-suited for PET imaging and has a half-life of 12.7 h, allowing adequate elimination of nonspecific radioactivity from background tissues.[26] Currently, methods for labeling HFn with copper-64 include utilizing the inherent properties of HFn (disassembly and reassembly, metal cation channels, etc.)[27] as well as genetic modification of the interior surface of HFn for internal loading or chelation of copper-64.[28] However, these interior-loading methods may impact the encapsulation of other therapeutic drugs within HFn. Bifunctional chelators (such as NOTA and DOTA) play a crucial role in connecting radioactive metal nuclides to targeting carriers.[29] By modification of the outer surface of HFn with these dual-functional chelators through the free lysine residues, copper-64 can be efficiently labeled onto HFn. This chelator-protein labeling method does not occupy the internal cavity of HFn, allowing for the loading of other drugs

and thus offering advantages for combination therapy. Therefore, in this study, a novel radiopharmaceutical named [^{64}Cu]Cu-NOTA-HFn was synthesized to validate its ability to target NPC with high CD71 expression, potentially guiding further personalized treatment for recurrent and metastatic distant NPC.

2. MATERIALS AND METHODS

2.1. General Information. HFn was generously provided by the group of Prof. Kelong Fan from the Institute of Biophysics, Chinese Academy of Sciences. The crystal structure of HFn is identified by the PDB code 3AJO. Graphical visualizations were created using PyMOL (Schrodinger, Version 1.7.2.1). The human NPC cell line C666-1, uncontaminated with HeLa and from undifferentiated NPC,[30,31] was procured from FuHeng Cell Center (Shanghai, China). HK-1 cells, uncontaminated with HeLa and from well-differentiated squamous carcinoma,[31,32] were obtained from Central South University Advanced Research Center. Undifferentiated carcinomas represent the majority of cases in endemic areas and have a higher incidence of distant metastasis than differentiated squamous carcinomas.[3]

2.2. Cell Culture. NPC cell lines (C666-1, HK-1) were cultivated in 10 cm cell culture dishes (Corning, USA) using RPMI-1640 medium (Gibco, USA) supplemented with 10% fetal bovine serum (FBS, Moregate Biotech, New Zealand) and 1% penicillin-streptomycin (Gibco, USA). The cultures were maintained at 37 °C with 5% CO_2. Cell passaging was performed exclusively through trypsin-EDTA (Gibco, USA) digestion when the cell confluence reached 80%.

2.3. Western Blotting Analysis of CD71 Expression. CD71 expression of NPC cell lines (C666-1, HK-1) was investigated with Western Blotting Analysis. Cells at the logarithmic growth phase were lysed on ice for 30 min with a RIPA lysis buffer (Beyotime Biotechnology, China). The resultant proteins were heated at 100 °C for 10 min and separated on a 4−20% Bis-Tris SurePAGE Gel (GenScript, USA). Following gel electrophoresis, the proteins were transferred onto PVDF membranes and were incubated with a 1:500 dilution of rabbit antihuman CD71 polyclonal antibody (Sigma-Aldrich, USA) on a shaker at 4 °C overnight. After washing and incubating with HRP-conjugated goat antirabbit secondary antibody (Invitrogen, USA) at room temperature for 1 h, the immunoblot signal was subsequently detected using the ChemiDoc XRS+ gel imaging system (Bio-Rad Laboratories, USA) via enhanced chemiluminescence (Biosharp, China). Densitometric analysis was conducted using ImageJ software (National Institutes of Health, USA).

2.4. Fluorescence Microscopy Analysis of CD71 Expression and the Uptake of HFn-FITC. Fluorescence microscopy analysis was used to show the colocalization of CD71 and HFn-FITC within CD71-positive C666-1 cells. Upon reaching 90% confluence, C666-1 cells were detached, washed, and then fixed with 4% paraformaldehyde for 15 min at 37 °C. After washing and suspending in phosphate-buffered saline (PBS), a 20 μL aliquot of the cell suspension was placed onto a slide, allowed to sit for 20 min at room temperature, and then dried in an oven at 37 °C. The cell smears were permeabilized with 0.1% Triton X-100 for 15 min and blocked with 3% bovine serum albumin (BSA) for 1 h at room temperature. The cells were then incubated with the following reagents: 5 μg/mL of mouse IgG1 kappa isotype control (Invitrogen, USA), 5 μg/mL of CD71 mouse monoclonal

antibody (Invitrogen, USA), and 10 μg/mL of HFn-FITC in 0.1% BSA at 4 °C overnight. Subsequently, the cells were labeled with Alexa Fluor 488 and Alexa Fluor 555 secondary goat antimouse antibody (Bioss, China) at a dilution of 1:100 for 1 h at room temperature. After rinsing with PBS containing 0.05% tween 20 (Solarbio, China), an antifade mounting medium with DAPI (Beyotime Biotechnology, China) was applied to stain the cell nuclei for 10 min. Finally, the cell smears were examined using a confocal laser scanning microscope with 405, 488, and 543 nm wavelengths of laser (Zeiss LSM880, Carl Zeiss AG, Oberkochen, Germany).

2.5. Flow Cytometry Analysis of CD71 Expression and the Uptake of HFn-FITC. Flow cytometry analysis was used to assess the CD71 expression and uptake of HFn-FITC in C666-1 cells. Detached cell suspensions (2.5×10^6 cells per mL, 100 μL) were stained with FITC-conjugated HFn at a concentration of 20 μg/mL, mouse IgG1 kappa isotype control at 5 μg/mL, and CD71 mouse monoclonal antibody (OKT9) at 5 μg/mL for 1 h at 4 °C in PBS containing 0.3% BSA, respectively. After washing in cold PBS, cells were incubated with Alexa Fluor 555 secondary goat antimouse antibody at a dilution of 1:100 for 30 min at 4 °C. After rinsing and resuspending, cells were immediately analyzed using a flow cytometer (CytoFLEX LX, Beckman Coulter, IN, USA). To evaluate whether HFn binding to C666-1 was specific and how it changes with time, the cell uptake assay of Cy5.5-HFn was conducted (detailed in Supplementary Information).

2.6. Radiolabeling, In Vitro Stability, and Hydrophilicity of [⁶⁴Cu]Cu-NOTA-HFn. HFn was conjugated with p-SCN-Bn-NOTA (Macrocyclics, USA) in 0.1 M NaHCO₃ at pH 9.0, maintaining a NOTA to HFn molar ratio of 10:1, 20:1, and 40:1. The reaction mixture was allowed to proceed at room temperature for approximately 2 h, followed by gentle overnight stirring at 4 °C. The average number of NOTA per HFn at different feed ratios (detailed in Supplementary Information) was determined by using the spectroscopic assay. The affinity of NOTA-HFn in comparison to HFn was tested by ELISA assay (detailed in Supplementary Information). Subsequently, purification was accomplished through dialysis in a sodium acetate buffer (0.2 M, pH 5.2). To initiate the process, 185 MBq of [⁶⁴Cu]CuCl₂ (Beijing Atomic High Tech Radiopharmaceutical Co., Ltd., China) was introduced into a 1.5 mL Eppendorf tube containing 250 μL of sodium acetate buffer with the precursor NOTA-HFn (4 mg/mL). The mixture was incubated at 40 °C for 15 min. Radio-TLC (Elysia-Raytest, Straubenhardt, Germany) was employed to monitor the radiochemical conversion on TLC-SG chromatography paper (Agilent Technologies, USA) developed with 10 mM ethylenediaminetetraacetic acid (EDTA). We named the product obtained [⁶⁴Cu]Cu-NOTA-HFn, according to the consistent nomenclature conventions of radiopharmaceutical chemistry.[33]

The in vitro stability of [⁶⁴Cu]Cu-NOTA-HFn was evaluated in PBS. For this assessment, [⁶⁴Cu]Cu-NOTA-HFn (22.2 MBq, 100 μL) was added into 100 μL of PBS (0.1 M) at 37 °C. Subsequently, the stability of [⁶⁴Cu]Cu-NOTA-HFn at 15 min, 1, 2, 3, 4, 5, 6, 10, 14, 18, 25, and 48 h was quantified using radio-TLC. The stability of [⁶⁴Cu]Cu-NOTA-HFn in FBS is detailed in Supplementary Information.

A total of 50 μL of [⁶⁴Cu]Cu-NOTA-HFn (0.185 MBq) was introduced into a solution composed of 450 μL of PBS and 500 μL of 1-octanol. The mixture underwent vortexing at room temperature for 5 min and was subsequently subjected to

centrifugation at 10,000 g for 10 min. Following centrifugation, the radioactivity concentrations in 200 μL samples extracted from both the aqueous and organic phases were quantified using a gamma counter (WIZARD, PerkinElmer Instruments, USA). The partition coefficient (Log P) values were calculated and expressed as mean ± SD ($n = 6$), with Log P = log (the organic phase counts/the aqueous phase counts).

2.7. Saturation Binding Assay. C666-1 cells were incubated with serial dilutions of [⁶⁴Cu]Cu-NOTA-HFn at concentrations ranging from 0.025 to 6.17 nM for 30 min at 4 °C. For the block group, the cells were saturated with a 100-fold excess of nonradiolabeled HFn for 2 h before adding [⁶⁴Cu]Cu-NOTA-HFn. After being washed with PBS, the adherent cells were lysed with 1 M NaOH at room temperature for 5 min. The cell lysates and residues were collected and detected by the gamma counter (WIZARD, PerkinElmer, Waltham, USA) to obtain count per min (CPM). The total binding of [⁶⁴Cu]Cu-NOTA-HFn was from the CPM of the nonblock group, and the nonspecific binding was from the CPM of the block group. The specific binding of [⁶⁴Cu]Cu-NOTA-HFn was calculated by subtracting CPM nonspecific binding from CPM total binding. The dissociation constant (K_d) was calculated by curve fitting with a one-site saturation binding model using GraphPad Prism 8.4.3 (GraphPad Software, La Jolla, USA).

2.8. Animal PET/CT Imaging, Ex Vivo Imaging and Biodistribution. All animal experiments were conducted following the ethical guidelines and under the supervision of the Institutional Animal Care and Use Committee (IACUC) at the Fifth Affiliated Hospital of Sun Yat-sen University (animal protocol No. # 00309). Four-week-old BALB/c nude male mice were housed under specific-pathogen-free conditions at the Guangdong Provincial Engineering Research Center of Molecular Imaging. The animal tumor model was established through subcutaneous injection of approximately 5×10^6 C666-1 cells suspended in 125 μL of PBS into the right thigh of the mice. The length and width of the resulting tumors, measured in millimeters using calipers, were used to calculate tumor volume as follows: tumor volume (mm³) = length × width²/2. When the average tumor volume reached about 100 mm³, the mice were randomly assigned to different experimental groups.

A total of eight nude mice bearing C666-1 cell tumors were randomly divided into two groups: the nonblock group ($n = 4$) and the block group ($n = 4$). They were intravenously injected with 125 μL of [⁶⁴Cu]Cu-NOTA-HFn at a radioactivity dose of 11.1 MBq. In the block group, 36-fold the concentration of nonradiolabeled HFn was injected 6 h before the administration of the radiotracer. PET/CT imaging studies were conducted using a nanoPET/CT scanner (Mediso, Hungary) equipped with computer-controlled vertical and horizontal chamber motion. Images were acquired 1, 6, 12, 24, and 36 h after tracer injection. The mice were anesthetized with 2.0% isoflurane to maintain spontaneous breathing during imaging. The mean standardized uptake values (SUV) for tissues of interest, including the tumor, heart, blood, lung, liver, kidney, and muscle, were quantified from PET/CT data using Carimas analysis software (Turku, Finland). The uptake of the blood was obtained by drawing on the ascending aorta as the region of interest. At the end of the in vivo PET/CT imaging study, mice ($n = 2$) were euthanized for ex vivo imaging. Various tissues, including blood, heart, lungs, muscles, brain, bone, liver, kidneys, spleen, pancreas, intestine, stomach, and tumor,

were promptly dissected and subjected to ex vivo PET/CT imaging with a 10 min static scan.

To confirm differences in the biodistribution of $[^{64}Cu]Cu$-NOTA-HFn in tumor tissues between the nonblock group ($n = 3$) and the block group ($n = 3$), the biodistribution test was conducted at 6 h postinjection (p.i.). The above major tissues were weighed and assessed for radioactivity using the gamma counter. The results were expressed as the percentage of uptake of the injected dose per gram of tissue (%ID/g).

2.9. Histopathological Staining. To validate the expression and distribution of CD71 and confirm the binding specificity of HFn to C666-1 tumor tissues and tissue samples of NPC patients, hematoxylin-eosin (HE) staining, immuno-histochemical (IHC) staining, and immunofluorescence (IF) staining were performed. This research received approval from the Medical Ethics Committee of the Fifth Affiliated Hospital of Sun Yat-sen University (Approval Number: K129-1). Tumor tissue samples were initially fixed with 4% paraformaldehyde to prepare paraffin-embedded tissue sections. For HE, tumor sections (4 μm) were stained with hematoxylin solution for 5 min and eosin solution for 3 min.

For the IHC analysis, rabbit antihuman CD71 polyclonal antibody (Sigma-Aldrich, USA) was utilized at a dilution of 1:500 and incubated at 4 °C overnight, followed by HRP-conjugated goat antirabbit IgG secondary antibody (Invitrogen, USA) for 30 min at 37 °C. After incubating with freshly prepared DAB substrate (ZSGB-BIO, China), tissue samples underwent counterstaining with hematoxylin. The sections were scanned by using a Pannoramic 250 Flash II digital scanner (3DHISTECH Inc., Budapest, Hungary).

For IF, tissue sections were concurrently incubated with rabbit antihuman CD71 polyclonal antibody (Sigma-Aldrich, USA) at a 1:500 dilution and HFn-FITC (10 μg/mL) or HFn-Cy5.5 (10 μg/mL) at 4 °C overnight. The negative control was treated with rabbit IgG (Bioss, China) instead of the primary antibody. Subsequently, the sections were labeled with Alexa Fluor 555 secondary goat antirabbit antibody (Bioss, China) at a 1:100 dilution for 1 h at room temperature. After counterstained with DAPI, the stained tissues were examined using a confocal laser scanning microscope.

2.10. Statistical Analysis. Quantitative data were expressed as the mean ± standard deviation (SD). All statistical analyses were performed using GraphPad Prism version 8.4.3 statistical software. Nonparametric tests (Mann−Whitney test) were employed for non-normally distributed data analysis, and unpaired, two-tailed Student's t-test for normally distributed data analysis, with statistical significance set at $p < 0.05$.

3. RESULTS

3.1. CD71 Expression in NPC Cell Lines and Cell Uptake of HFn-FITC. The Western blotting results showed that both C666-1 and HK-1 cells, uncontaminated with HeLa, were overexpressed CD71 (Figure 1a,b, $n = 3$), indicating that maybe both undifferentiated and differentiated cells could express CD71. Given that undifferentiated carcinomas are the predominant cases in endemic regions and exhibit a greater propensity for distant metastasis when compared to differentiated carcinomas,[3] C666-1 was selected for subsequent investigations. The confocal test demonstrated the colocalization of anti-CD71 and HFn with a colocalization coefficient of 0.67 ± 0.10 ($n = 3$) (Figure 1c). The binding activity of HFn-FITC to C666-1 cells was confirmed by flow cytometric analysis (Figure 1d), which illustrated that HFn-FITC strongly
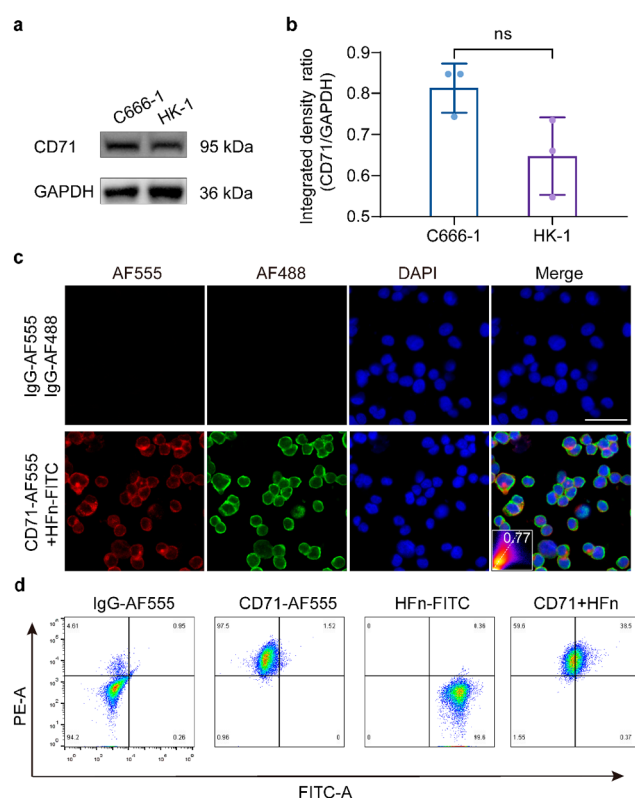
Figure 1. CD71 expression in NPC cell lines and cell uptake of HFn-FITC. (a,b) Western blotting of CD71 expressions in C666-1 and HK-1 (a), and quantification of CD71 expressions presented as the ratio of CD71 vs GAPDH (b). (c) Representative fluorescence images of C666-1 incubated with IgG, anti-CD71 + HFn-FITC, respectively, with a scale bar of 40 μm. The colocalization coefficient in the shown image is 0.77. (d) Flow cytometry analysis of the cellular uptake of IgG, anti-CD71, HFn-FITC, and anti-CD71 + HFn-FITC, respectively. The data of (b) are expressed as mean ± SD and the Mann−Whitney test was used to calculate the p value. "ns" not significant.

bound to C666-1, demonstrating the ability of HFn to recognize C666-1 NPC cells. Besides, the binding could be inhibited by anti-CD71 as the binding site of the anti-CD71 we used is also located at the apical domain of CD71 and may partially overlap with the binding site of HFn to CD71.[34] The cell uptake assay indicated the specific cellular uptake of Cy5.5-HFn in vitro (Figure S3).

3.2. Radiolabeling of $[^{64}Cu]Cu$-NOTA-HFn and Cell Saturation Binding Assay. The ratios of NOTA to HFn in different feed ratios are shown in Table S1. There was no noteworthy difference in the affinity of NOTA-HFn in comparison to HFn (Figure S1). Radiolabeling of NOTA-HFn (the feed ratio of 10:1) with $[^{64}Cu]CuCl_2$ was successful with high yield (>98.5%, $n = 3$, 2a,b) and molar activity (72.96 ± 21.33 GBq/μmol, $n = 3$). The in vitro solubility and stability tests revealed that $[^{64}Cu]Cu$-NOTA-HFn had a high water solubility (Log $P = -2.42 \pm 0.52$, $n = 6$) and good stability in PBS and FBS (Figure 2c, S2). The cell saturation binding assay demonstrated that the cell binding rate increased gradually with increasing concentration of $[^{64}Cu]Cu$-NOTA-HFn (Figure 2d). The one-site saturation binding curve and Scatchard plot demonstrated that HFn bound to C666-1 cells with a high affinity (K_d of 10.9 ± 6.1 nM, $n = 3$) (Figure 2e).
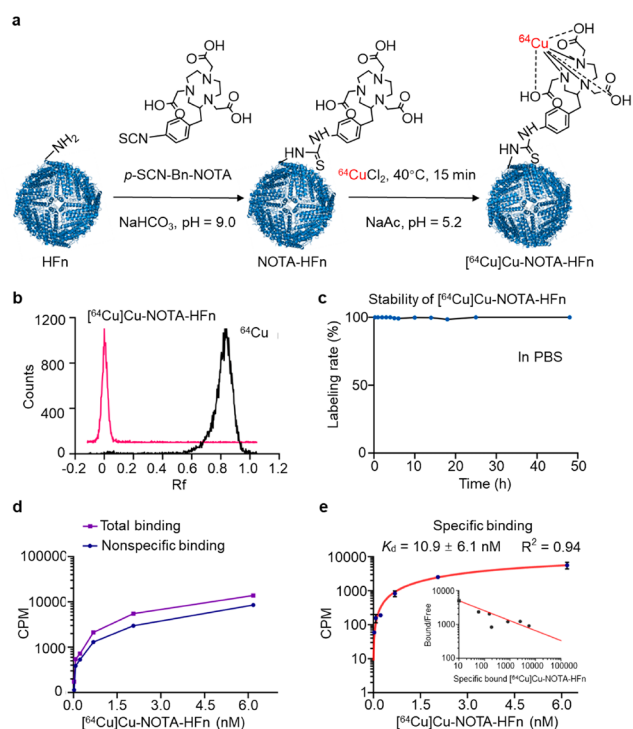
Figure 2. Synthesis of $[^{64}Cu]$Cu-NOTA-HFn and cell saturation binding of $[^{64}Cu]$Cu-NOTA-HFn. (a) Labeling scheme of $[^{64}Cu]$Cu-NOTA-HFn. (b) Radio-TLC of copper-64 and $[^{64}Cu]$Cu-NOTA-HFn. (c) In vitro stability of $[^{64}Cu]$Cu-NOTA-HFn in PBS within 48 h. (d) $[^{64}Cu]$Cu-NOTA-HFn specific binding to C666-1 cells, which could be blocked by excess nonradiolabeled HFn. (e) One-site saturation binding curve and Scatchard plot showed the binding affinity of $[^{64}Cu]$Cu-NOTA-HFn to C666-1 cells ($K_d = 10.9 \pm 6.1$ nM, $n = 3$).

3.3. Tumor-Bearing Mice PET/CT Imaging, Ex Vivo Imaging and Biodistribution.

To verify the target engagement in vivo, PET imaging was performed at 1, 6, 12, 24, and 36 h p.i. of $[^{64}Cu]$Cu-NOTA-HFn to the C666-1 tumor-bearing mice (Figure 3a), and representative images were obtained (Figure 3b). The C666-1 tumors were most visible with high contrast to the contralateral background at 6 h. The tracer revealed receptor-specific tumor accumulation, which was illustrated by effective blocking via injection with excess nonradiolabeled HFn. Furthermore, quantitative analysis of the time-activity curve for the tumor revealed that the uptake of $[^{64}Cu]$Cu-NOTA-HFn in C666-1 tumors increased over time, peaking at 6 h and then declining (Figure 3c). The SUVs of tumors in the nonblock group were 2.00, 2.33, 1.87, 1.55, and 1.44 times of the block group at 1, 6, 12, 24, and 36 h, respectively ($n = 4$, $p < 0.05$). In addition, the tumor-to-blood (T/B) ratios at 6, 12, 24, and 36 h (Figure 3d) and the tumor-to-muscle (T/M) ratios at each scanning time point (Figure 3e) in C666-1 tumors of the nonblock group also showed significantly higher than the block group in vivo through PET/CT imaging ($n = 4$, $p < 0.05$). For the ex vivo imaging, the radioactivity intensity of tumors and major organs was similar to that for the in vivo imaging at 36 h p.i. (Figure 3f,g). The difference in biodistribution of $[^{64}Cu]$Cu-NOTA-HFn in tumor tissues between nonblock and block groups was confirmed by the biodistribution at 6 h p.i. (Figure 3h), which was consistent with the quantitative analysis of PET/CT imaging.
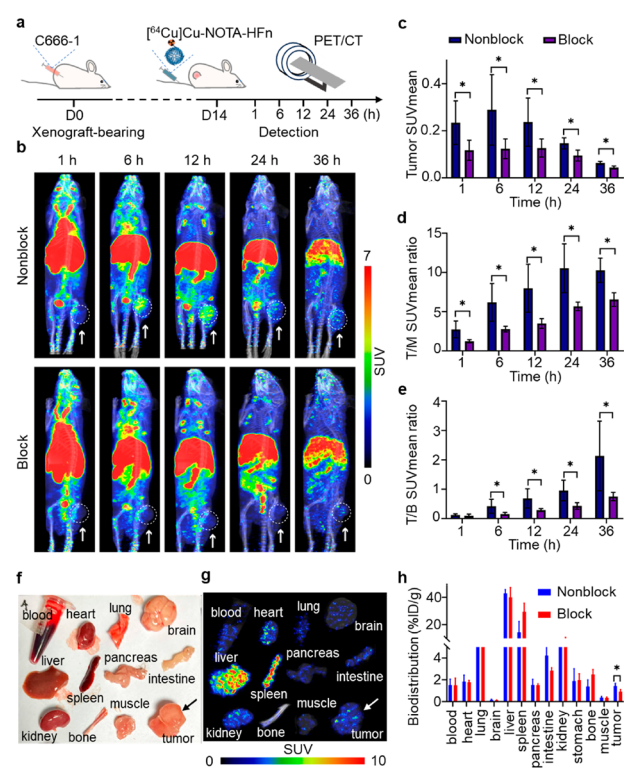
Figure 3. Tumor-bearing mice PET/CT imaging, ex vivo imaging, and biodistribution. (a) Flowchart for PET/CT imaging of $[^{64}Cu]$Cu-NOTA-HFn in C666-1 xenograft models. (b) Representative whole-body Maximum Intensity Projection (MIP) PET/CT images of $[^{64}Cu]$Cu-NOTA-HFn in C666-1 tumor-bearing mice at 1, 6, 12, 24, and 36 h p.i. The upper row is the nonblock group, and the bottom row is the block group. The dotted circles and white arrows refer to the tumor. (c,e) Quantitative analysis of PET/CT imaging of $[^{64}Cu]$Cu-NOTA-HFn ($n = 4$). (c) Time−activity curve of tumor uptake from 1 to 36 h. (d) Tumor-to-muscle (T/M) ratios in mice postinjection. (e) Tumor-to-blood (T/B) ratios in mice postinjection. (f) Ex vivo photograph of interesting organs, the black arrow refers to the tumor. Photograph courtesy of Yanfang Shen. Copyright 2024. (g) PET imaging of ex vivo organs, the white arrow refers to the tumor. (h) Biodistribution of the $[^{64}Cu]$Cu-NOTA-HFn after 6 h p.i. uptake ($n = 3$). The data are expressed as mean ± SD. Mann−Whitney test in (c−e) and unpaired, two-tailed Student's t-test in (f) were used to calculate p values. *$p < 0.05$.

3.4. Histopathological Staining.

The results of HE, IHC, and IF staining confirmed the expression of CD71 and the uptake of HFn in C666-1 cells of xenograft tumors on BALB/c nude mice and NPC tissues of patients. Representative images are shown in Figure 4. HE staining for the mice tumor tissues is shown in Figure 4a. The adjacent sections demonstrated positive CD71 expression within the cytoplasm and on the cell membranes of tumor tissues (Figure 4b). Similarly, HFn-FITC and HFn-Cy5.5 were also observed within the cytoplasm and cell membranes of tumor tissues of C666-1 tumor-bearing mice and NPC patients (Figure 4c,d).

4. DISCUSSION

Recurrent and metastatic NPC constitutes the primary reason for treatment failure. Identifying effective biomolecular targets and developing targeted probes hold promise for early and specific tumor diagnosis as well as guiding individualized therapies. CD71, a type II transmembrane glycoprotein
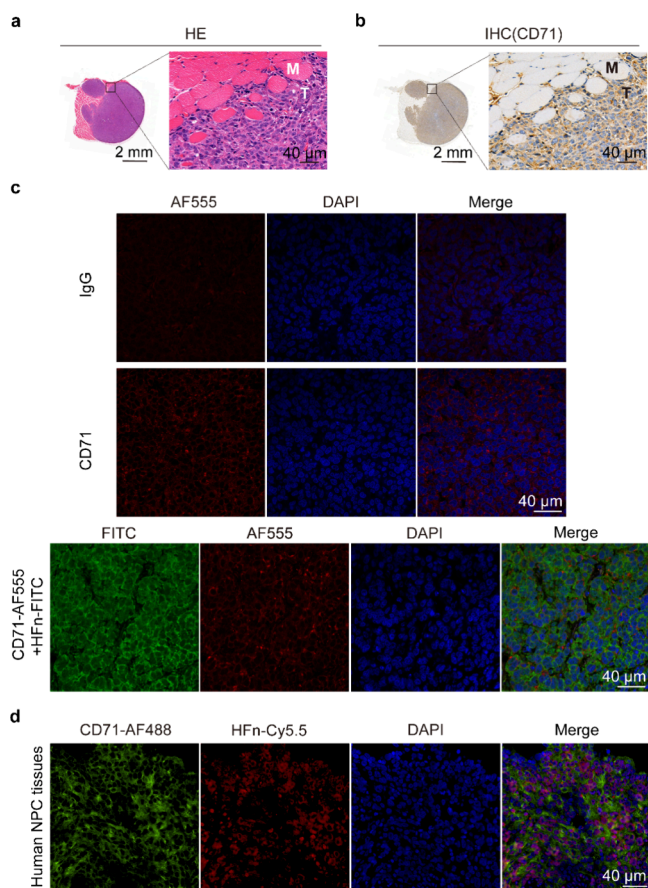
Figure 4. Histopathological confirmation of tumor tissues of C666-1 tumor-bearing mice and NPC patients: HE (a), IHC (b), and IF (c) staining of C666-1 cells of xenograft tumors; IF (d) staining of NPC tissues of patients. (a) HE staining of tumors and adjacent muscle tissues, with a scale bar of 2 mm for the overall image and 40 μm for the enlarged view. (b) IHC staining of tumors and adjacent muscle tissues for the expression of CD71, with a scale bar of 2 mm for the overall image and 40 μm for the enlarged view. "T" denotes tumor, and "M" represents muscle. (c) IF staining of mice tumor tissues with IgG, anti-CD71, and anti-CD71 + HFn-FITC, respectively. (d) IF staining of NPC tissues of patients with anti-CD71 + HFn-Cy5.5 (c,d) with a scale bar of 40 μm.

responsible for mediating cellular iron uptake, is commonly overexpressed within tumors. HFn, a natural and biocompatible iron storage protein, has been shown to bind to human cells via CD71.[22] In our study, high expression of CD71 and HFn-FITC uptake in NPC cells were confirmed through immunoblotting, flow cytometry, and cell IF assays. Based on these findings, we developed a novel radiotracer that targets CD71 using radionuclide-labeled HFn for noninvasive diagnosis of NPC.

Different from the previous interior-loading methods,[27,28] the p-SCN-Bn-NOTA was modified on free lysine residues of HFn, allowing loading with therapeutic drugs. The high radiochemical labeling rate and high in vitro stability of [^{64}Cu]Cu-NOTA-HFn were confirmed, which provided a fundamental basis for further translation or clinical applications. The [^{64}Cu]Cu-NOTA-HFn labeling route offers several advantages, such as a high radiochemical yield (higher than the loading rate reported in ref 27 which was 60%[27]), an effortless radiolabeled process, a short production time of 15 min (shorter than 1 h[27,28]), and good stability due to the inherently

stable nanocages structure of HFn. Besides the well-established coordination chemistry and high labeling efficiency of the [^{64}Cu]Cu-NOTA-HFn labeling route, the long-term imaging capability afforded by copper-64 provides an opportunity to model the retention and clearance kinetics in vivo beyond 24 h after tracer administration. With similar methods, multiple promising imaging isotopes such as zirconium-89, and therapeutic isotopes, such as lutetium-177, yttrium-90, and copper-67[35] can label HFn nanocages for different applications. Furthermore, due to the cage-like structure of HFn, a variety of drugs can be loaded into the inner lumen. Several studies have reported loading chemotherapy drugs such as doxorubicin[25] and cisplatin[36] to treat tumors. In the future, it is expected to realize the theranostics of cancer mediated by HFn.

Furthermore, [^{64}Cu]Cu-NOTA-HFn exhibited high binding affinity and specificity to C666-1 cells in vitro through the cell saturation binding assay. Animal studies proved the in vivo tumor-targeting specificity of [^{64}Cu]Cu-NOTA-HFn in NPC tumor-bearing mice. Up to date, there are limited options for tumor-specific PET imaging probes for NPC. A recent study[37] utilized [^{68}Ga]Ga-DOTA-TATE to target somatostatin receptor 2 (SSTR2), which is overexpressed in various tumors, including NPC. Through PET imaging, this study aimed to perform noninvasive diagnosis and screen patients for targeted therapy, which was achieved by covalently linking cytotoxic drugs with peptides that target SSTR2. Compared to the promising peptides used for integrating diagnosis and treatment, HFn is also a highly promising ligand due to its advantages. HFn is naturally present in the body thus with good biocompatibility and safety and is inherently targeted to CD71 without requiring any modifications. It can encapsulate drugs within its lumen with a high drug-loading capacity, which allows for effective tumor inhibition with a single dose.[25] HFn has been widely used as a CD71 ligand in the diagnosis and treatment of tumors.[23] However, there have been a few studies on the use of radionuclide-labeled HFn for tumors, with the main focus being on copper-64 and iodine-125. Wang et al.[38] used [^{64}Cu]CuS-ferritin nanocages to visualize xenograft tumors in mouse models of human glioma. The results showed that the peak probe uptake time was 8 h, which was similar to that in our study. Liang et al.[25] used [^{125}I]I-HFn-DOX to perform SPECT imaging in colon cancer tumor-bearing mice. The results showed that the probe still had obvious visualization in the tumor 24 h after injection, indicating that HFn may have a long tumor retention time, which will be beneficial for tumor treatment.

However, the relatively high levels of hepatic and splenic accumulation were still a major limitation to our study and further therapeutic experiments. From the available analysis, some reasons may be inferred. First, the increased hepatic uptake of copper-64 is most likely due to free radionuclides as macrocyclic copper chelates have limited in vivo stability of superoxide dismutase in the liver.[39,40] To prevent the dissociation of copper-labeled complex, new methods must be developed that can stop the reduction of the cupric ions or improve the coordination of the cuprous ions. It may be helpful to identify more chelators capable of stabilizing both copper states. For instance, sulfur-containing chelators were recently investigated as promising candidates for application in copper-based radiopharmaceuticals.[41] Second, the liver and spleen were the main organs for ferritin nanoparticle metabolism, thus exhibiting strong HFn accumulation.[25,42]

To effectively reduce the uptake of nanomaterials in the liver, a study by Tsoi et al.[43] suggested two promising approaches: (1) increasing the flow rate to decrease the probability of nanomaterial sequestration and (2) altering the phenotype of key cells to reduce their affinity for nanomaterials. Further confirmation is required to determine whether these methods can reduce HFn uptake in the liver and spleen.

To the best of our knowledge, this was the first report of [64Cu]Cu-NOTA-HFn for the preclinical evaluation of NPC. We demonstrated that noninvasive detection of CD71 expression by PET imaging with [64Cu]Cu-NOTA-HFn could be a modality for diagnosing NPC. Therefore, we will further optimize the probe to improve the target-to-nontarget ratio for future clinical applications in patients with CD71-overexpressing tumors.

5. CONCLUSIONS

We synthesized a new radioligand, [64Cu]Cu-NOTA-HFn, with a high radiochemical labeling rate. PET imaging with [64Cu]Cu-NOTA-HFn showed that the radioligand can specifically bind to CD71 receptors in CD71-positive NPC tumors. Our study provided a foundation for future studies to exploration of radionuclides labeled HFn for clinical application in patients with CD71-overexpressing tumors.

■ ASSOCIATED CONTENT

ⓢ Supporting Information

The Supporting Information is available free of charge at https://pubs.acs.org/doi/10.1021/acsomega.4c00187.

> NOTA-to-HFn ratios; the affinity of NOTA-HFn compared with HFn to CD71; the stability of [64Cu]Cu-NOTA-HFn in FBS; in vitro cell uptake of Cy5.5-HFn; and in vivo fluorescence imaging of Cy5.5-HFn (PDF)

■ AUTHOR INFORMATION

Corresponding Authors

Hongjun Jin − *Guangdong Provincial Engineering Research Center of Molecular Imaging, The Fifth Affiliated Hospital and Guangdong-Hong Kong-Macao University Joint Laboratory of Interventional Medicine, The Fifth Affiliated Hospital, Sun Yat-sen University, Zhuhai 519000, China;* ⓞ orcid.org/0000-0002-1522-1098; Email: jinhj3@mail.sysu.edu.cn

Ying Wang − *Department of Nuclear Medicine, The Fifth Affiliated Hospital, Sun Yat-sen University, Zhuhai 519000, China;* ⓞ orcid.org/0000-0002-7922-9064; Email: wangy9@mail.sysu.edu.cn

Authors

Yanfang Shen − *Department of Nuclear Medicine, The Fifth Affiliated Hospital, Guangdong Provincial Engineering Research Center of Molecular Imaging, The Fifth Affiliated Hospital, and Guangdong-Hong Kong-Macao University Joint Laboratory of Interventional Medicine, The Fifth Affiliated Hospital, Sun Yat-sen University, Zhuhai 519000, China*

Renwei Zhou − *Department of Nuclear Medicine, The Fifth Affiliated Hospital, Guangdong Provincial Engineering Research Center of Molecular Imaging, The Fifth Affiliated Hospital, and Guangdong-Hong Kong-Macao University Joint Laboratory of Interventional Medicine, The Fifth*
Affiliated Hospital, Sun Yat-sen University, Zhuhai 519000, China

Lei Bi − *Guangdong Provincial Engineering Research Center of Molecular Imaging, The Fifth Affiliated Hospital and Guangdong-Hong Kong-Macao University Joint Laboratory of Interventional Medicine, The Fifth Affiliated Hospital, Sun Yat-sen University, Zhuhai 519000, China*

Guolong Huang − *Guangdong Provincial Engineering Research Center of Molecular Imaging, The Fifth Affiliated Hospital and Guangdong-Hong Kong-Macao University Joint Laboratory of Interventional Medicine, The Fifth Affiliated Hospital, Sun Yat-sen University, Zhuhai 519000, China*

Min Yang − *Department of Nuclear Medicine, The Fifth Affiliated Hospital, Guangdong Provincial Engineering Research Center of Molecular Imaging, The Fifth Affiliated Hospital, and Guangdong-Hong Kong-Macao University Joint Laboratory of Interventional Medicine, The Fifth Affiliated Hospital, Sun Yat-sen University, Zhuhai 519000, China*

Zhijun Li − *Guangdong Provincial Engineering Research Center of Molecular Imaging, The Fifth Affiliated Hospital and Guangdong-Hong Kong-Macao University Joint Laboratory of Interventional Medicine, The Fifth Affiliated Hospital, Sun Yat-sen University, Zhuhai 519000, China*

Jijin Yao − *Guangdong Provincial Engineering Research Center of Molecular Imaging, The Fifth Affiliated Hospital and Guangdong-Hong Kong-Macao University Joint Laboratory of Interventional Medicine, The Fifth Affiliated Hospital, Sun Yat-sen University, Zhuhai 519000, China*

Jianzhong Xian − *Guangdong Provincial Engineering Research Center of Molecular Imaging, The Fifth Affiliated Hospital and Guangdong-Hong Kong-Macao University Joint Laboratory of Interventional Medicine, The Fifth Affiliated Hospital, Sun Yat-sen University, Zhuhai 519000, China*

Yifan Qiu − *Guangdong Provincial Engineering Research Center of Molecular Imaging, The Fifth Affiliated Hospital and Guangdong-Hong Kong-Macao University Joint Laboratory of Interventional Medicine, The Fifth Affiliated Hospital, Sun Yat-sen University, Zhuhai 519000, China*

Peizhen Ye − *Guangdong Provincial Engineering Research Center of Molecular Imaging, The Fifth Affiliated Hospital and Guangdong-Hong Kong-Macao University Joint Laboratory of Interventional Medicine, The Fifth Affiliated Hospital, Sun Yat-sen University, Zhuhai 519000, China*

Yongshan Liu − *Guangdong Provincial Engineering Research Center of Molecular Imaging, The Fifth Affiliated Hospital and Guangdong-Hong Kong-Macao University Joint Laboratory of Interventional Medicine, The Fifth Affiliated Hospital, Sun Yat-sen University, Zhuhai 519000, China*

Yuyi Hou − *Guangdong Provincial Engineering Research Center of Molecular Imaging, The Fifth Affiliated Hospital and Guangdong-Hong Kong-Macao University Joint Laboratory of Interventional Medicine, The Fifth Affiliated Hospital, Sun Yat-sen University, Zhuhai 519000, China*

Complete contact information is available at:
https://pubs.acs.org/10.1021/acsomega.4c00187

Notes

The authors declare no competing financial interest.

REFERENCES

(1) Chen, Y.; Chan, A. T. C.; Le, Q.; Blanchard, P.; Sun, Y.; Ma, J. Nasopharyngeal carcinoma. *Lancet* **2019**, *394*, 64−80.

(2) Almobarak, A. A.; Jebreel, A. B.; Abu-Zaid, A. Molecular Targeted Therapy in the Management of Recurrent and Metastatic Nasopharyngeal Carcinoma: A Comprehensive Literature Review. *CUREUS* **2019**, *11*, No. e4210, DOI: 10.7759/cureus.4210.

(3) Wei, W. I.; Sham, J. S. Nasopharyngeal carcinoma. *Lancet* **2005**, *365*, 2041−2054.

(4) Lee, A. W. M.; Ma, B. B. Y.; Ng, W. T.; Chan, A. T. C. Management of Nasopharyngeal Carcinoma: Current Practice and Future Perspective. *J. Clin. Oncol.* **2015**, *33*, 3356−3364.

(5) Dagogo-Jack, I.; Shaw, A. T. Tumour heterogeneity and resistance to cancer therapies. *Nat. Rev. Clin. Oncol.* **2018**, *15*, 81−94.

(6) King, A. D.; Woo, J.; Ai, Q. Y.; Chan, J.; Lam, W.; Tse, I.; Bhatia, K. S.; Zee, B.; Hui, E. P.; Ma, B.; et al. Complementary roles of MRI and endoscopic examination in the early detection of nasopharyngeal carcinoma. *Ann. Oncol.* **2019**, *30*, 977−982.

(7) Weissleder, R.; Pittet, M. J. Imaging in the era of molecular oncology. *Nature* **2008**, *452*, 580−589.

(8) Herschman, H. R. Molecular imaging: looking at problems, seeing solutions. *Science* **2003**, *302*, 605−608.

(9) Mammatas, L. H.; Verheul, H. M.; Hendrikse, N. H.; Yaqub, M.; Lammertsma, A. A.; Menke-van, D. H. V. O. Molecular imaging of targeted therapies with positron emission tomography: the visualization of personalized cancer care. *Cell. Oncol. (Dordr.)* **2015**, *38*, 49−64.

(10) Marx, S.; Dal Maso, T.; Chen, J. W.; Bury, M.; Wouters, J.; Michiels, C.; Le Calve, B. Transmembrane (TMEM) protein family members: Poorly characterized even if essential for the metastatic process. *Semin. Cancer Biol.* **2020**, *60*, 96−106.

(11) Dowling, P.; Walsh, N.; Clynes, M. Membrane and membrane-associated proteins involved in the aggressive phenotype displayed by highly invasive cancer cells. *Proteomics* **2008**, *8*, 4054−4065.

(12) Gammella, E.; Buratti, P.; Cairo, G.; Recalcati, S. The transferrin receptor: the cellular iron gate. *Metallomics* **2017**, *9*, 1367−1375.

(13) Shen, Y.; Li, X.; Dong, D.; Zhang, B.; Xue, Y.; Shang, P. Transferrin receptor 1 in cancer: a new sight for cancer therapy. *Am. J. Cancer Res.* **2018**, *8*, 916−931.

(14) Singh, M.; Mugler, K.; Hailoo, D. W.; Burke, S.; Nemesure, B.; Torkko, K.; Shroyer, K. R. Differential expression of transferrin receptor (TfR) in a spectrum of normal to malignant breast tissues: implications for in situ and invasive carcinoma. *Appl. Immunohistochem Mol. Morphol* **2011**, *19*, 417−423.

(15) Fu, Y.; Lin, L.; Xia, L. MiR-107 function as a tumor suppressor gene in colorectal cancer by targeting transferrin receptor 1. *Cell. Mol. Biol. Lett.* **2019**, *24*, 31.

(16) Wu, H.; Zhang, J.; Dai, R.; Xu, J.; Feng, H. Transferrin receptor-1 and VEGF are prognostic factors for osteosarcoma. *J. Orthop. Surg. Res.* **2019**, *14*, No. 296, DOI: 10.1186/s13018-019-1301-z.

(17) Adachi, M.; Kai, K.; Yamaji, K.; Ide, T.; Noshiro, H.; Kawaguchi, A.; Aishima, S. Transferrin receptor 1 overexpression is associated with tumour de-differentiation and acts as a potential prognostic indicator of hepatocellular carcinoma. *Histopathology* **2019**, *75*, 63−73.

(18) Moon, S. J.; Kim, J. H.; Kong, S. H.; Shin, C. S. Protein Expression of Cyclin B1, Transferrin Receptor, and Fibronectin Is Correlated with the Prognosis of Adrenal Cortical Carcinoma. *Endocrinol Metab (Seoul)* **2020**, *35*, 132−141.

(19) Feng, G.; Arima, Y.; Midorikawa, K.; Kobayashi, H.; Oikawa, S.; Zhao, W.; Zhang, Z.; Takeuchi, K.; Murata, M. Knockdown of TFRC suppressed the progression of nasopharyngeal carcinoma by down-regulating the PI3K/Akt/mTOR pathway. *Cancer Cell Int.* **2023**, *23*, 185.

(20) Pirollo, K. F.; Nemunaitis, J.; Leung, P. K.; Nunan, R.; Adams, J.; Chang, E. H. Safety and Efficacy in Advanced Solid Tumors of a Targeted Nanocomplex Carrying the p53 Gene Used in Combination with Docetaxel: A Phase 1b Study. *Mol. Ther.* **2016**, *24*, 1697−1706.

(21) Song, X.; Liang, C.; Feng, L.; Yang, K.; Liu, Z. Iodine-131-labeled, transferrin-capped polypyrrole nanoparticles for tumor-targeted synergistic photothermal-radioisotope therapy. *Biomater Sci.* **2017**, *5*, 1828−1835.

(22) Montemiglio, L. C.; Testi, C.; Ceci, P.; Falvo, E.; Pitea, M.; Savino, C.; Arcovito, A.; Peruzzi, G.; Baiocco, P.; Mancia, F.; et al. Cryo-EM structure of the human ferritin-transferrin receptor 1 complex. *Nat. Commun.* **2019**, *10*, 1121.

(23) He, J.; Fan, K.; Yan, X. Ferritin drug carrier (FDC) for tumor targeting therapy. *J. Controlled Release* **2019**, *311*, 288−300.

(24) Kawabata, H. Transferrin and transferrin receptors update. *Free Radic Biol. Med.* **2019**, *133*, 46−54.

(25) Liang, M.; Fan, K.; Zhou, M.; Duan, D.; Zheng, J.; Yang, D.; Feng, J.; Yan, X. H-ferritin-nanocaged doxorubicin nanoparticles specifically target and kill tumors with a single-dose injection. *Proceedings of the National Academy of Sciences - PNAS* **2014**, *111*, 14900−14905.

(26) Ahmedova, A.; Todorov, B.; Burdzhiev, N.; Goze, C. Copper radiopharmaceuticals for theranostic applications. *Eur. J. Med. Chem.* **2018**, *157*, 1406−1425.

(27) Lin, X.; Xie, J.; Niu, G.; Zhang, F.; Gao, H.; Yang, M.; Quan, Q.; Aronova, M. A.; Zhang, G.; Lee, S.; et al. Chimeric Ferritin Nanocages for Multiple Function Loading and Multimodal Imaging. *Nano Lett.* **2011**, *11*, 814−819.

(28) Zhang, J.; Cheng, D.; He, J.; Hong, J.; Yuan, C.; Liang, M. Cargo loading within ferritin nanocages in preparation for tumor-targeted delivery. *Nat. Protoc.* **2021**, *16*, 4878−4896.

(29) Roosenburg, S.; Laverman, P.; Joosten, L.; Cooper, M. S.; Kolenc-Peitl, P. K.; Foster, J. M.; Hudson, C.; Leyton, J.; Burnet, J.; Oyen, W. J.; et al. PET and SPECT imaging of a radiolabeled minigastrin analogue conjugated with DOTA, NOTA, and NODAGA and labeled with (64)Cu, (68)Ga, and (111)In. *Mol. Pharmaceutics* **2014**, *11*, 3930−3937.

(30) Cheung, S. T.; Huang, D. P.; Hui, A. B.; Lo, K. W.; Ko, C. W.; Tsang, Y. S.; Wong, N.; Whitney, B. M.; Lee, J. C. Nasopharyngeal carcinoma cell line (C666−1) consistently harbouring Epstein-Barr virus. *Int. J. Cancer* **1999**, *83*, 121−126.

(31) Chan, S. Y.; Choy, K. W.; Tsao, S. W.; Tao, Q.; Tang, T.; Chung, G. T.; Lo, K. W. Authentication of nasopharyngeal carcinoma tumor lines. *Int. J. Cancer* **2008**, *122*, 2169−2171.

(32) Huang, D. P.; Ho, J. H.; Poon, Y. F.; Chew, E. C.; Saw, D.; Lui, M.; Li, C. L.; Mak, L. S.; Lai, S. H.; Lau, W. H. Establishment of a cell line (NPC/HK1) from a differentiated squamous carcinoma of the nasopharynx. *Int. J. Cancer* **1980**, *26*, 127−132.

(33) Coenen, H. H.; Gee, A. D.; Adam, M.; Antoni, G.; Cutler, C. S.; Fujibayashi, Y.; Jeong, J. M.; Mach, R. H.; Mindt, T. L.; Pike, V. W.; et al. Consensus nomenclature rules for radiopharmaceutical chemistry - Setting the record straight. *Nucl. Med. Biol.* **2017**, *55*, v−xi.

(34) Ferrero, S.; Flores, M. D.; Short, C.; Vazquez, C. A.; Clark, L. E.; Ziegenbein, J.; Zink, S.; Fuentes, D.; Payes, C.; Batto, M. V.; et al. Antibody-Based Inhibition of Pathogenic New World Hemorrhagic Fever Mammarenaviruses by Steric Occlusion of the Human Transferrin Receptor 1 Apical Domain. *J. Virol.* **2021**, *95*, No. e186820.

(35) Mikolajczak, R.; van der Meulen, N. P.; Lapi, S. E. Radiometals for imaging and theranostics, current production, and future perspectives. *J. Labelled Comp Radiopharm* **2019**, *62*, 615−634.

(36) Pontillo, N.; Pane, F.; Messori, L.; Amoresano, A.; Merlino, A. Cisplatin encapsulation within a ferritin nanocage: a high-resolution crystallographic study. *Chem. Commun. (Camb)* **2016**, *52*, 4136−4139.

(37) Lechner, M.; Schartinger, V. H.; Steele, C. D.; Nei, W. L.; Ooft, M. L.; Schreiber, L. M.; Pipinikas, C. P.; Chung, G. T.; Chan, Y. Y.; Wu, F.; et al. Somatostatin receptor 2 expression in nasopharyngeal cancer is induced by Epstein Barr virus infection: impact on prognosis, imaging and therapy. *Nat. Commun.* **2021**, *12*, 117.

(38) Wang, Z.; Huang, P.; Jacobson, O.; Wang, Z.; Liu, Y.; Lin, L.; Lin, J.; Lu, N.; Zhang, H.; Tian, R.; et al. Biomineralization-Inspired Synthesis of Copper Sulfide-Ferritin Nanocages as Cancer Theranostics. *ACS Nano* **2016**, *10*, 3453−3460.

(39) Bass, L. A.; Wang, M.; Welch, M. J.; Anderson, C. J. In vivo transchelation of copper-64 from TETA-octreotide to superoxide dismutase in rat liver. *Bioconjug Chem.* **2000**, *11*, 527−532.

(40) Watabe, T.; Liu, Y.; Kaneda-Nakashima, K.; Shirakami, Y.; Lindner, T.; Ooe, K.; Toyoshima, A.; Nagata, K.; Shimosegawa, E.; Haberkorn, U.; et al. Theranostics Targeting Fibroblast Activation Protein in the Tumor Stroma: (64)Cu- and (225)Ac-Labeled FAPI-04 in Pancreatic Cancer Xenograft Mouse Models. *J. Nucl. Med.* **2020**, *61*, 563−569.

(41) Tosato, M.; Dalla, T. M.; May, N. V.; Isse, A. A.; Nardella, S.; Orian, L.; Verona, M.; Vaccarin, C.; Alker, A.; Macke, H.; et al. Copper Coordination Chemistry of Sulfur Pendant Cyclen Derivatives: An Attempt to Hinder the Reductive-Induced Demetalation in (64/67)Cu Radiopharmaceuticals. *Inorg. Chem.* **2021**, *60*, 11530−11547.

(42) Liang, M.; Tan, H.; Zhou, J.; Wang, T.; Duan, D.; Fan, K.; He, J.; Cheng, D.; Shi, H.; Choi, H. S.; et al. Bioengineered H-Ferritin Nanocages for Quantitative Imaging of Vulnerable Plaques in Atherosclerosis. *ACS Nano* **2018**, *12*, 9300−9308.

(43) Tsoi, K. M.; MacParland, S. A.; Ma, X. Z.; Spetzler, V. N.; Echeverri, J.; Ouyang, B.; Fadel, S. M.; Sykes, E. A.; Goldaracena, N.; Kaths, J. M.; et al. Mechanism of hard-nanomaterial clearance by the liver. *Nat. Mater.* **2016**, *15*, 1212−1221.